Astronomy & Astrophysics manuscript no. output
February 28, 2020

WASP-33A and b revealed by TESS

Phase curve and secondary eclipse from the planet, and pulsations from the star

C. von Essen[1,2], M. Mallonn[3], C. C. Borre[1], and G. Tautvaišienė[2]

[1] Stellar Astrophysics Centre, Department of Physics and Astronomy, Aarhus University, Ny Munkegade 120, DK-8000 Aarhus C, Denmark
e-mail: cessen@phys.au.dk
[2] Astronomical Observatory, Institute of Theoretical Physics and Astronomy, Vilnius University, Sauletekio av. 3, 10257, Vilnius, Lithuania
[3] Leibniz-Institut für Astrophysik Potsdam (AIP), An der Sternwarte 16, D-14482 Potsdam, Germany

Received —-; accepted —-

ABSTRACT

We present the detection and characterization of the secondary eclipse and the phase curve of the ultra-hot Jupiter WASP-33b, along the in-detailed determination of the pulsation spectrum of the host star. To this end, we analyzed data collected by the Transiting Exoplanet Survey Satellite (TESS) during Sector 18. WASP-33b belongs to a very short list of highly irradiated exoplanets that were discovered from the ground and were afterwards visited by TESS. WASP-33b's host star, of δScuti type, shows non-radial pulsations in the milli-magnitude regime, with periods comparable to that of the primary transit. These completely deform the photometric light curves, hindering our interpretations from them. Carrying out a detailed characterization of the pulsation spectrum of the host star, we find 29 pulsations with signal-to-noise ratio higher than 4. After cleaning the light curve for the stellar pulsations we confidently report a secondary eclipse depth of 425 ± 32 parts-per-million (ppm), along with an amplitude of the phase curve of 100 ± 12 ppm and a corresponding offset between the region of maximum brightness and the substellar point of -13.6 ± 6.2 degrees. This, in combination with our derived bond albedo, $A_B = 0.239 \pm 0.039$, and heat recirculation efficiency, $\epsilon = 0.191 \pm 0.007$, reconfirm WASP-33b to be similar in behaviour to other hot Jupiters, despite the high irradiation received from its host star. Connecting the amplitude of the phase curve to the primary transit and secondary eclipse depths we determine the day and night-side brightness temperatures of WASP-33b to be 3184 ± 43 K and 1702 ± 22 K, respectively, making WASP-33b one of the few planets having a set of three brightness temperatures determined, one of such pairs derived in this work. Analyzing the stellar pulsations in the frame of the planetary orbit we find no signals of star-planet interactions.

Key words. stars: planetary systems – stars: individual: WASP-33 – methods: observational

1. Introduction

Since August, 2018, the Transiting Exoplanet Survey Satellite (TESS Ricker et al. 2015) has been scanning the southern and northern ecliptic hemispheres in the search for planets around bright stars. To date (March, 2020), TESS has detected the dim of light during transit of ∼1700 TESS Objects of Interest (TOIs), out of which ∼40 have been confirmed as exoplanets[1]. Several TESS discoveries include the first Earth-sized planet (Dragomir et al. 2019), an eccentric massive Jupiter orbiting a sub giant star each 9.5 days (Rodriguez et al. 2019), and the first multi-planet systems (Kostov et al. 2019; Günther et al. 2019; Vanderburg et al. 2019).

Besides the detection and characterization of brand-new systems, TESS has also been contributing with the in-depth study of those previously detected from the ground. Some of TESS contributions are the detection of a decrease in the orbital period of WASP-4b (Bouma et al. 2019), and of particular interest to this work, the characterization of the phase curve and secondary eclipse depth of WASP-19b (Wong et al. 2019a), WASP-18b (Shporer et al. 2019), WASP-121b (Bourrier et al. 2019; Daylan et al. 2019) and KELT-9b (Wong et al. 2019b). For WASP-18b, the precision in the photometry allowed Shporer et al. (2019) to unveil sinusoidal modulations across the orbital phase, that were shaped by the atmospheric characteristics of the planet and by the gravitational interactions between planet and host star. WASP-19b's data revealed a strong atmospheric brightness modulation signal and no significant offset detected between the substellar point and the region of maximum brightness on the day-side of the planet, in full agreement with what WASP-121b data showed. It is clear from these discoveries, that TESS is at its full potential to unveil the orbital phase curves of transiting exoplanets.

One particular aspect that all the previously mentioned exoplanets share is their high brightness temperature. Also showing this particular feature, the ultra-hot Jupiter WASP-33b (Collier Cameron et al. 2010) was also observed by TESS. So far, WASP-33b is at the very top of a short list of highly irradiated, super hot exoplanets, as the planet orbits a δ Scuti star of spectral type A, that oscillates with pulsations commensurable to the transit duration and with amplitudes well within the milli-magnitude regime (Smith et al. 2011; Herrero et al. 2011; von Essen et al. 2014). So far, the planet has been thoughtfully investigated. Among others, observational data have revealed several secondary eclipse depths at different wavelengths (Smith et al. 2011; Deming et al. 2012; de Mooij et al. 2013; Haynes et al. 2015; von Essen et al. 2015), a detailed characterization

[1] https://tess.mit.edu/publications/

of the pulsation spectrum of the host star with the goal of determining planetary parameters from pulsation-cleaned light curves (Herrero et al. 2011; von Essen et al. 2014), and the characterization of its atmospheric composition where aluminium oxide was for the first time ever unveiled (von Essen et al. 2019). In addition, space-based observations of WASP33's phase curves in the near infrared (Zhang et al. 2018) allowed the authors to estimate the planetary brightness temperature, albedo and recirculation efficiency, finding WASP-33b to behave more like a hot Jupiter, despite its unusually high irradiation level.

In this work we investigate the phase curve of WASP-33b provided by TESS twenty three days of continuous monitoring. We show in Section 2 a detailed description of the observations used to characterize the secondary eclipse and the phase curve of WASP-33b. In Section 3 we dive into our results, where we present our analysis over the third light contamination (Section 3.1), our update on the transit parameters (Section 3.2) and our strategy to clean the light curves from transits to use them to determine the pulsation spectrum of the host star (Section 3.3). We introduce our models to interpret WASP-33b's secondary eclipse and phase curve in Section 3.5. Once these are determined, and the impact of the pulsations on the derived values is well investigated (Section 4.1) we finish this work with some conclusive remarks under Section 5.

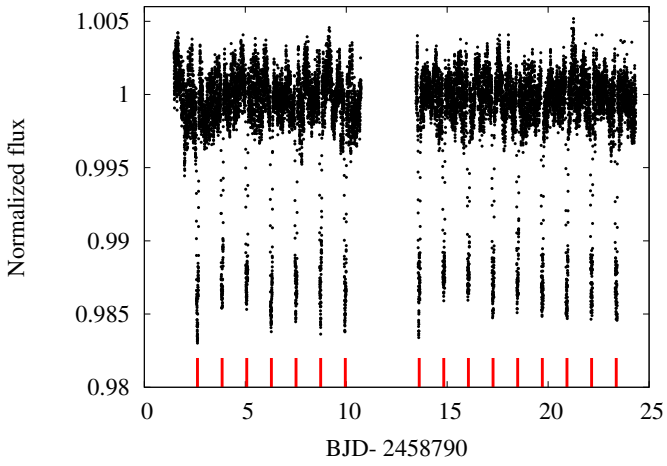

Fig. 1: Normalized flux of WASP-33 observed by TESS in black circles. The pulsations of the star deform the continuum level. The sixteen transits are indicated in the bottom of the figure with red lines. The gap in the middle is caused by data download dead time.

2. Observations

WASP-33 (TIC identifier 129979528) was observed by TESS during sector 18, more specifically during November 3^{nd} and 26^{th}, 2019, during cycle 2 and using camera 1. The data have a cadence of 120 seconds and were analyzed and detrended by the Science Processing Operations Center (SPOC) pipeline, based on the NASA Kepler mission pipeline (Jenkins et al. 2016; Jenkins 2017). Time stamps are given in Barycentric Julian Date (BJD_{TDB}), and are in consequence not converted to other time reference frame.

The light curve of WASP-33 can be seen in Figure 1. The total time on target is of about 23 days, during which 16 primary transits were observed. These are indicated with red lines in the bottom of the figure. The first ~800 data points were not considered in our analysis, as they show noise structure that we believe is extrinsic to the star.

In this work we present an analysis over the photometry provided by the TESS team, more specifically the light curve provided by the PDC msMAP correction method.

3. Results

3.1. Third light contamination

When analyzing photometric time series including exoplanetary primary transits, special care has to be taken. In certain cases, light of another star than the planetary host is included inside the chosen photometric aperture, diluting the depth of the primary transits (TBD: add citations). TESS cameras have a pixel size of 21×21 arcseconds. Under these circumstances, when a light curve is constructed co-adding the light of several pixels (see Figure 2, *top*) it is very likely that the aperture will include light from other stars than that of the host (Figure 2, *bottom*).

WASP-33's first identified companion, WASP-33B, lies at an angular separation of ~2 arcseconds and is, in consequence, included inside TESS aperture. The sub-stellar object was first reported by Moya et al. (2011) and then confirmed by Adams et al. (2013); Wöllert & Brandner (2015); Ngo et al. (2016). Using years of follow-up observations, Ngo et al. (2016) carried out a combined analysis and pinpointed WASP-33 as a binary system candidate. Nowadays, WASP-33 has been identified as a hierarchical triple star system (Mugrauer 2019) with a second companion, WASP-33C, ~49 arcseconds away from the planet-host star. Owed to its orientation (South-East from WASP-33), WASP-33C is not included inside TESS aperture. A third star, located 23 arcseconds North-West from WAP-33 (Gaia DR2 3286360240205710 08, Gaia Collaboration et al. 2018, G = 14.6173 ± 0.0005) is included. In consequence, prior to the transit fitting we computed the third light contribution of WASP-33's companions within TESS transmission response, namely that of WASP-33B and Gaia DR2 3286360240205710 08.

Due to the nature of the system it is safe to assume WASP-33 and WASP-33B to be at the same distance. In consequence, we reproduced their emission with PHOENIX synthetic spectra (Göttingen 2018) without the need of scaling the fluxes further to account for distances. As PHOENIX spectra we used those with stellar values effective temperature, T_{eff}, metallicity, [Fe/H], and surface gravity, log(g), closely matching the corresponding values of WASP-33 (Collier Cameron et al. 2010) and of the close-in companion (Ngo et al. 2016). Their values are summarized in Table 1. After convolving PHOENIX intensities with TESS transmission response, we integrated the remaining fluxes and computed their ratio. In this fashion, the third light contribution of WASP-33B is $F_{W33B}/F_{W33} = 0.018$.

The case of Gaia DR2 3286360240205710 08 is slightly different as it is not bound to WASP-33 by gravity, not allowing us to assume equal distances. Gaia Collaboration et al. (2018) estimated its temperature to be ~5075 K, so we represented its emission using PHOENIX synthetic spectra for a main sequence star of T_{eff} = 5000 K. To compensate for the difference in distance, we computed Gaia's magnitude difference between WASP-33 (G = 8.0700 ± 0.0004) and this star, and we scaled PHOENIX flux ratios of WASP-33 and Gaia DR2 3286360240205710 08 integrated within Gaia's transmission response to meet the magnitude difference. Then, we used this factor to scale down the spectra inside TESS transmission response. Like this, the

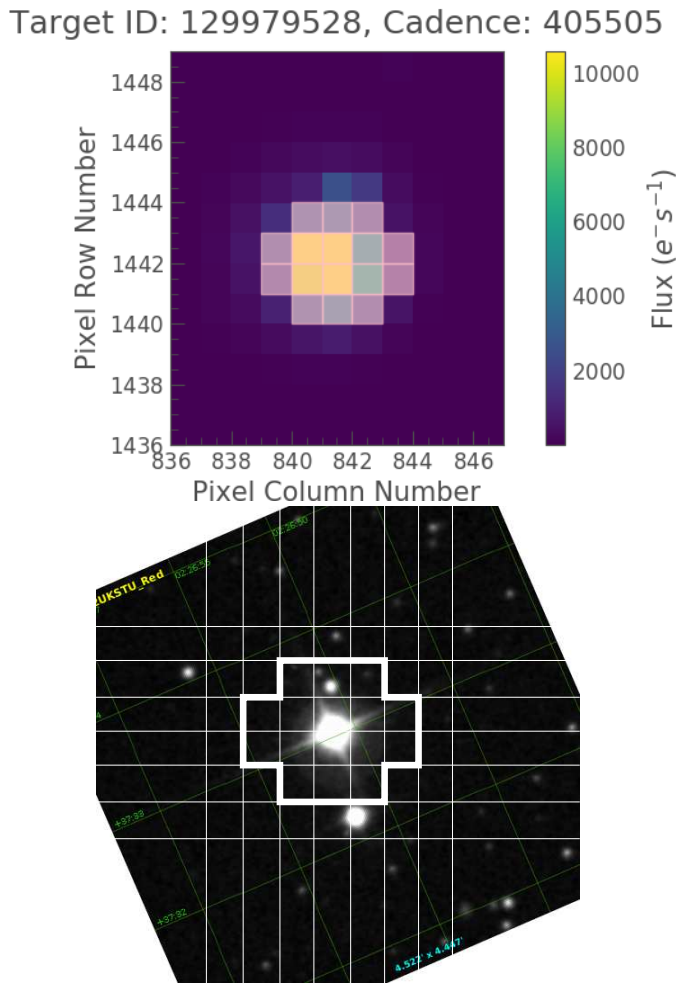

Fig. 2: *Top:* Target Pixel File (TPF) of WASP-33 showing the chosen aperture mask. No stars can be visually resolved. *Bottom:* ∼4×4 arcmin field of view centered around WASP-33. The mask and the pixels are schematized with white thick and thin lines, respectively. WASP-33C, the bright star south from WASP-33, is not included in the aperture. The field of view has been rotated to be aligned with the ecliptic system.

third light contribution of Gaia DR2 3286360240205710 08 is $F_{\rm Gaia}/F_{\rm W33} = 0.006$. The final third light contribution used in our model is the addition of these two.

3.1.1. Limb-darkening coefficients

In this work we adopted a quadratic limb-darkening law:

$$\frac{I(\mu)}{I(1)} = 1 - u_1(1-\mu) - u_2(1-\mu)^2, \quad (1)$$

with corresponding linear (u_1) and quadratic (u_2) limb-darkening coefficients (LDCs). In the equation, $I(1)$ is the specific intensity at the centre of the stellar disk and $\mu = \cos(\gamma)$, where γ is the angle between the line of sight and the emergent intensity. To compute our custom limb-darkening coefficients that meet TESS transmission response we used angle-dependent, specific intensity spectra from PHOENIX (Göttingen 2018) with main stellar parameters corresponding to the effective temperature, $T_{\rm eff}$ = 7400 K, surface gravity, log(g) = 4.5, and metallicity, [Fe/H] = 0.00, closely matching the values of WASP-33 reported in Table 1. Similarly done as von Essen et al. (2017) and Claret & Bloemen (2011), we neglect the data points between $\mu = 0$ and $\mu = 0.064$, as the intensity drop given by PHOENIX models is too steep and potentially unrealistic. After integrating the PHOENIX angle-dependent spectra convolved by TESS response, we fitted the derived intensities normalized by its maximum values with Equation 1 with a simple least-square minimization method. The derived limb-darkening coefficients for WASP-33 are $u_1 = 0.236(3)$ and $u_2 = 0.184(3)$. Errors for the coefficients are derived from χ^2 maps, choosing the values of the LDCs at which $\Delta\chi^2 = 1$. Throughout this work, limb-darkening coefficients are considered as fixed.

3.2. Primary transit

Even though the pulsations are evident in the transit light curves (see Figure A.1 and Figure A.2), in von Essen et al. (2014) we derived the transit parameters taking and not taking the intrinsic variability of the host star into consideration as part of the model budget, finding no significant differences in both derived set of transit parameters. In consequence, to clean WASP-33's photometry from transits to proceed afterwards with the determination of the pulsation spectrum of the host star and to update the transit parameters of the system, we fitted the photometry with a Mandel & Agol (2002) transit model only. The fitting parameters are the semi-major axis, a/R_S, the inclination in degrees, i, the orbital period, Per, the planet-to-star radius ratio, R_P/R_S, and the mid-transit time of reference, T_0. In this work we consider the eccentricity fixed and equal to zero (Smith et al. 2011).

To derive the best-fit values for the model parameters and their corresponding uncertainties we used a Markov-chain Monte Carlo (MCMC) approach, all implemented in routines of PyAstronomy[2] (Patil et al. 2010; Jones et al. 2001). We iterated 1 000 000 times, with a conservative burn-in of the first 20% samples. For all the parameters we considered uniform priors around ±50% their corresponding starting values, that were in turn taken from von Essen et al. (2014), specified in Table 2. We computed the mean and standard deviation from the posterior distributions, and used these as our best-fit values and uncertainties, given at 1-σ level. We checked the convergency of the chains by visually inspecting each one of them, and by dividing the chains in three sub-chains. In each case, we computed the usual statistics and we considered that a chain converged if the derived parameters were consistent within their uncertainties. The transit parameters presented in this work are, as expected given the nature of the data, slightly more precise and in most of the cases consistent at 1 or 2-σ level with bibliographic values.

The posterior distributions and the corresponding correlations between parameters can be seen in Figure 3. Besides the well known correlation between a/R_S and i, the remaining parameters are uncorrelated, with Pearson's correlation values ranging between -0.05 and 0.04.

3.3. Pulsation spectrum of the host star

The pulsations of the host star were determined using Period04 (Lenz & Breger 2005). The software uses a Fast Fourier Transform to calculate the power spectrum, and least square fitting to derive the frequencies, the amplitudes and the phases of the pulsations. These were extracted one by one, starting with the one having the largest amplitude. We considered a pulsation as

[2] www.hs.uni-hamburg.de/DE/Ins/Per/Czesla/PyA/PyA/index.html

Table 1: Basic stellar parameters effective temperature, metallicity and surface gravity, for WASP-33 and the stars included in TESS aperture.

Parameter	WASP-33 (Collier Cameron et al. 2010)	WASP-33B (Ngo et al. 2016)	Gaia DR2 328636024020571008 Gaia Collaboration et al. (2018)
T_{eff} (K)	7430 ± 100	3050 ± 250	5074.75
[Fe/H]	0.1 ± 0.2	0 (addopted)	0 (addopted)
log(g)	4.3 ± 0.2	5 (Angelov 1996)	4.5 (Angelov 1996)

Table 2: Best-fit transit parameters obtained from TESS photometry (this work), compared to those determined by von Essen et al. (2014), ignoring pulsations.

Parameter	This work	von Essen et al. (2014)
a/R_S	3.638 ± 0.002	3.69 ± 0.04
i (°)	89.85 ± 0.43	88.17 ± 1.53
R_P/R_S	0.11117 ± 0.00005	0.1052 ± 0.0004
Per (days)	1.2198740 ± 1.4×10^{-6}	1.2198667 ± 1.5×10^{-6}
T_0 (BJD_{TDB})	2458792.63391 ± 0.00002	2455507.5225 ± 0.0004

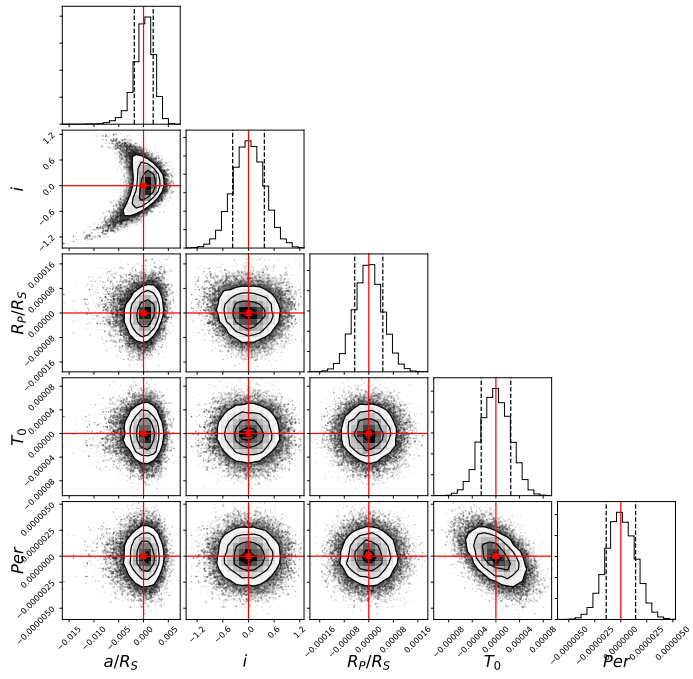

Fig. 3: Posterior distributions for the primary transit parameters fitted in this work. Gray to white contours indicate 1,2 and 3-σ intervals. The red points correspond to the best-fit values. The chains were shifted to the best-fit values of the parameters specified in Table 2, to allow for a better visual inspection of the uncertainties.

such if it was resolved, and if its corresponding signal-to-noise ratio was larger than 4 (see e.g., Breger et al. 1993; von Essen et al. 2014). In this calculation as "signal" we considered its amplitude, and as "noise" the averaged pulsation amplitudes over a frequency interval with a width of 2 c/d around each peak. We estimated the errors using Period04 MCMC's tool. The errors are produced as described in Breger et al. (1999), and are given in this work at 1-σ level. They were derived from 1000 MCMC iterations. Period04 fits all signals simultaneously. Since the errors on the amplitudes only depend on the fit-residuals and the number of data points in the time series, these are identical.

The power spectrum of WASP-33 is shown in Figure 4, and the 29 extracted pulsations are given in Table 3. For completeness, we provide a comparison to the pulsations found by von Essen et al. (2014).

Two signals from von Essen et al. (2014) were not reproduced in this analysis, namely 8.308 c/d ($Puls_7$) and 10.825 c/d ($Puls_8$). Both of them are located in a frequency region with high noise level in the TESS data. In consequence, it is not clear to us if the pulsations are present but obscured by the noise, or if they are not present at all. Stellar pulsations are excited and damped over time. In consequence, it might be possible that these pulsations were not excited during TESS timeline, but were during 2010-2012 (Aerts et al. 2010).

WASP-33 displays p-mode oscillations at high frequencies, which is characteristic for δ Scuti stars (see, e.g., Breger et al. 1995, 1996). Owed to the 23 days of continuous monitoring provided by TESS data, we also detected pulsations at lower frequencies (namely F2 and F5 on Table 3). These correspond to g-mode pulsations typical for γ Doradus stars (Breger & Montgomery 2000; Aerts et al. 2010). Showing both g and p-mode pulsations, WASP-33 would then fall into the γ Doradus/δ Scuti hybrid classification (Grigahcène et al. 2010; Balona & Dziembowski 2011; Uytterhoeven et al. 2011). However, with only two low-frequency pulsations detected, we are sceptic to classify the star as such. In von Essen et al. (2014), signals with frequencies lower than ~7 c/d where not detectable. Besides the obvious gaps produced by day time, the data were normalized on a nightly basis, removing in consequence the long trends. Also, due to poor weather conditions the observations could not be produced along consecutive nights, and had on average a ~5 hour duration. A longer time series than the one provided by TESS could resolve the pulsations at lower frequencies, and thereby determine if the star is purely a δ Scuti or a hybrid star.

3.4. Star-planet interaction

Compared to von Essen et al. (2014), the quality of TESS data allowed us to carry out a more thorough analysis of the pulsation spectrum of the host star. As now we count with almost 4 times more pulsations than those characterized before, we investigated again if any of the observed pulsations were induced by planetary tides over the star.

To begin with, the low-frequency domain of WASP-33's power spectrum does not reveal a ~4 c/d non-radial pulsation,

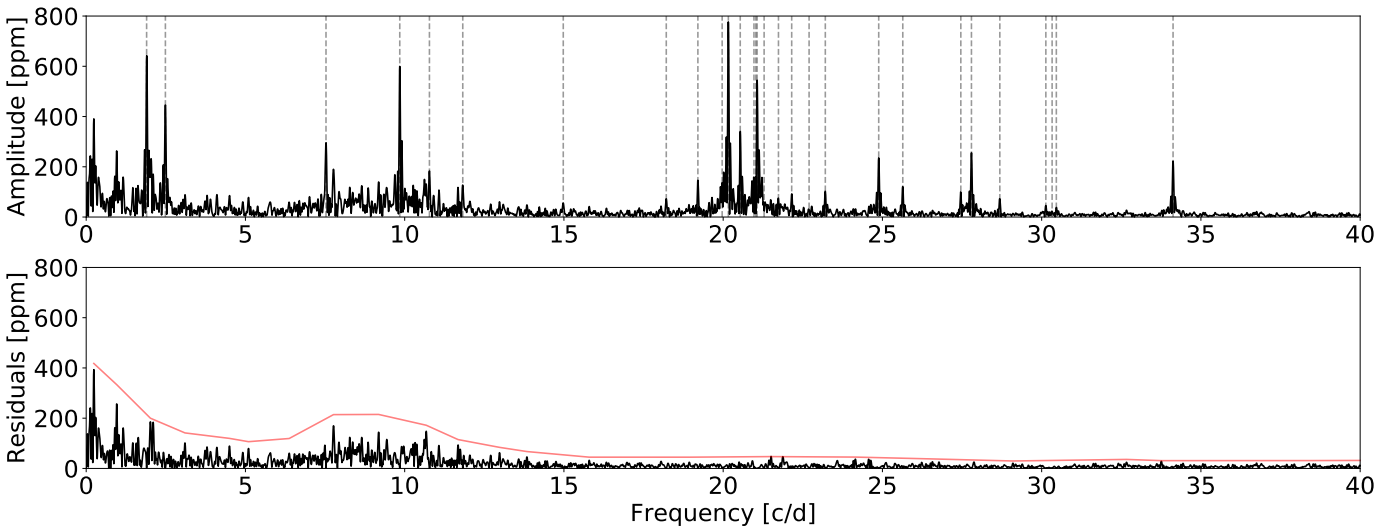

Fig. 4: Top panel: Power spectrum of WASP-33. Pulsations are marked with dashed gray lines. Bottom panel: Residuals after frequency extraction. The red line makes the SNR limit of 4.

Table 3: Pulsations of WASP-33 derived from TESS photometry. From left to right we present the frequency number, F#, arranged in decreasing amplitude, the frequency, in c/d, the amplitude, in ppm, the phase, in units of 2π, and the frequency, in c/per. In all cases errors are given at 1-σ level. The last column shows the frequencies obtained in von Essen et al. (2014), coinciding to the ones found here.

F#	Frequency (c/d)	Amplitude (ppm)	Phase (2π)	Frequency (c/per)	Frequency (von Essen et al. 2014, c/d)
F1	20.16263 ± 0.00032	772 ± 10	0.4904 ± 0.0020	24.59587	20.16214 ± 0.00063 ($Puls_1$)
F2	1.89739 ± 0.00038	648 ± 10	0.0084 ± 0.0024	2.31457	-
F3	9.84567 ± 0.00041	604 ± 10	0.4927 ± 0.0026	12.01047	9.84361 ± 0.00066 ($Puls_3$)
F4	21.06527 ± 0.00043	564 ± 10	0.3151 ± 0.0028	25.69697	21.06057 ± 0.00058 ($Puls_2$)
F5	2.48691 ± 0.00052	468 ± 10	0.6578 ± 0.0034	3.03371	-
F6	20.53605 ± 0.00073	334 ± 10	0.2175 ± 0.0047	25.05139	20.53534 ± 0.00057 ($Puls_5$)
F7	7.52946 ± 0.00083	296 ± 10	0.5895 ± 0.0053	9.18499	-
F8	27.79525 ± 0.00096	256 ± 10	0.9856 ± 0.0062	33.90670	-
F9	24.8835 ± 0.0010	243 ± 10	0.9808 ± 0.0065	30.35479	24.88351 ± 0.00056 ($Puls_4$)
F10	34.1254 ± 0.0011	220 ± 10	0.9392 ± 0.0072	41.62869	34.12521 ± 0.00054 ($Puls_6$)
F11	20.9668 ± 0.0012	198 ± 10	0.9824 ± 0.0080	25.57684	-
F12	10.7773 ± 0.0013	184 ± 10	0.0815 ± 0.0086	13.14690	-
F13	11.8238 ± 0.0019	130 ± 10	0.385 ± 0.012	14.42360	-
F14	25.6394 ± 0.0021	118 ± 10	0.854 ± 0.013	31.27689	-
F15	19.2058 ± 0.0021	116 ± 10	0.986 ± 0.014	23.42869	-
F16	23.2070 ± 0.0023	107 ± 10	0.075 ± 0.015	28.30967	-
F17	19.9681 ± 0.0024	104 ± 10	0.331 ± 0.015	24.35852	-
F18	27.4616 ± 0.0028	88 ± 10	0.165 ± 0.018	33.49973	-
F19	21.7361 ± 0.0031	80 ± 10	0.267 ± 0.020	26.51525	-
F20	22.1513 ± 0.0032	76 ± 10	0.686 ± 0.021	27.02181	-
F21	21.0256 ± 0.0034	72 ± 10	0.203 ± 0.022	25.64863	-
F22	28.68628 ± 0.0035	69 ± 10	0.127 ± 0.023	34.99365	-
F23	18.2134 ± 0.0036	69 ± 10	0.611 ± 0.023	22.21811	-
F24	21.2856 ± 0.0037	67 ± 10	0.064 ± 0.024	25.96576	-
F25	14.9793 ± 0.0045	55 ± 10	0.754 ± 0.029	18.27281	-
F26	30.1311 ± 0.0051	48 ± 10	0.415 ± 0.033	36.75612	-
F27	22.6975 ± 0.0052	47 ± 10	0.123 ± 0.034	27.68806	-
F28	30.4605 ± 0.0064	39 ± 10	0.585 ± 0.041	37.15799	-
F29	30.3283 ± 0.0088	28 ± 10	0.779 ± 0.056	36.99669	-

as previously reported by Collier Cameron et al. (2010). In addition to this, tidally excited modes can be manifested in two ways (see, e.g. Hambleton et al. 2013). These are given by the commensurability between the orbital period of the planet and a) the pulsation frequencies, and b) the spacing between the modes. Similarly to von Essen et al. (2014), we used our best-fit orbital period to express the pulsation frequencies as cycles per orbital period (c/per). These are given in the fifth column of Table 3. We found the closest commenurability to be 36.99669 c/per, corresponding to the frequency 30.3283 ± 0.0088 c/d. The difference to its closest integer number is equal to 0.00331. To assess if this difference is significant enough to pinpoint this pulsation as

being triggered by planetary tides, we carried out the same exercise as the one described in von Essen et al. (2014). Briefly, we randomly generate 29 frequencies between the lowest and the highest detected ones, that are in turn derived from a uniform distribution. Then, we convert these frequencies given in c/d to c/per, and among these we select the one closest to an integer number, computing their difference. We call this difference the "best match". After $1{\times}10^6$ iterations, we compute the cumulative probability distribution for the minimum distance from an integer frequency ratio as:

$$F(d_{min}) = 1 - e^{-d_{min}/v} \quad (2)$$

where v is obtained from fitting our Monte-Carlo results with an exponential decay (see Figure 5). The derived value is v = 0.0078 ± 0.0007. From this, we can determine that the probability of finding at least one of the ratios closer than 0.00331 c/per to an integer ratio, among 29 randomly produced pulsation frequencies, is 35%. This value is too high to confidentially claim this particular pulsation to be induced by the planet. In addition to this, no pair of pulsation spacings is an harmonic of the orbital period of the planet. In consequence, we find very unlikely that the system is showing evidences of star-planet interactions.

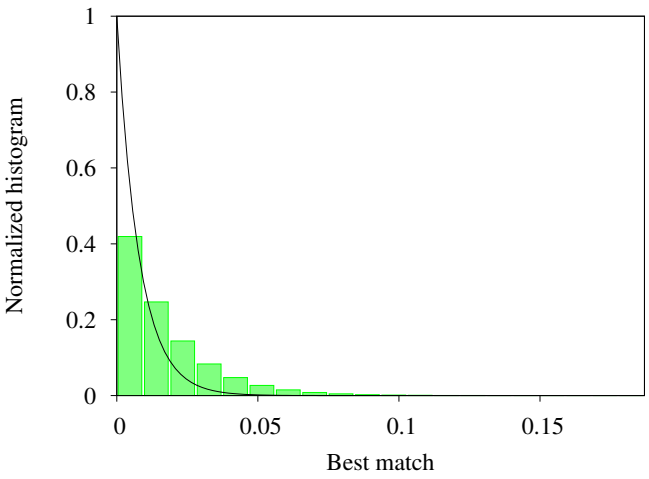

Fig. 5: Normalized histogram for the "best match" frequencies generated from 10^6 iterations.

3.5. Secondary eclipse and phase curve

As secondary eclipse model we considered a scaled version of the transit model given by Mandel & Agol (2002), with both linear and quadratic limb-darkening coefficients set to zero. The contribution of WASP-33's companion and the orbital eccentricity were considered in the same fashion as specified before. As described in von Essen et al. (2019), the secondary eclipse model, SEM(t), is given by:

$$\mathrm{SEM(t)} = [\mathrm{TM(t)} - 1.] \times \mathrm{sf} + 1, \quad (3)$$

where TM(t) corresponds to Mandel & Agol (2002)'s primary transit model, and sf corresponds to a scaling factor that scales the transit to meet the secondary eclipse depth. From this factor, the secondary eclipse depth is computed as $(\mathrm{R_P/R_s})^2 \times \mathrm{sf}$, and its error is computed from error propagation between the two. Due to the challenges imposed by the small intrinsic variability we are trying to tackle in a data set that is obscured by the pulsations of the host star, the only fitting parameter is the scaling factor. The rest of the parameters are completely connected to the primary transit model or are known with a high degree of precision from the literature. In consequence, they are considered as fixed.

As performed by, e.g., Cowan & Agol (2008) and Zhang et al. (2018) on WASP-33's Spitzer photometry, we modelled the planetary phase variability, PPV(t), as a series of first order expansions in sines and cosines:

$$\mathrm{PPV(t)} = c_0 + c_1 \times \sin(2\pi \mathrm{t/Per}) + c_2 \times \cos(2\pi \mathrm{t/Per}). \quad (4)$$

The fitting parameters are the offset, c_0, and the amplitudes of the sine and cosine, c_1 and c_2, respectively. The orbital period is considered as fixed to that obtained from the primary transit fitting.

Our combined model is then the addition of the secondary eclipse and the phase curve models, SEM(t) + PPV(t), that was fitted to the unbinned TESS photometry, once the primary transits and the most prominent pulsations were removed (see next Section). Equivalently to the primary transit fitting approach, to derive the best-fit values (sf, c_0, c_1 and c_2), we made use of MCMC. In this case, we iterated 10 000 times, with a burn-in of the first 2500 samples, after visually inspecting the chains for convergency. The best-fit values for the parameters, along with their corresponding 1-σ uncertainties, are derived from the mean and standard deviation of the posterior distributions.

4. Discussion

4.1. Impact of the pulsations over the derived secondary eclipse depth and phase curve amplitude

As reported in Section 3.3, 29 pulsations showed a significant signal above the noise and were, in consequence, detected as such. From Period04 we extracted the corresponding frequencies, amplitudes and phases, that were used to clean the data from pulsations to recover the planetary signature. To do so, similarly to von Essen et al. (2014, 2015) we considered the following pulsation model, PM(t):

$$\mathrm{PM(t)} = \sum_{\mathrm{i}=1}^{29} \mathrm{A_i} \times \sin[2\pi(\mathrm{t}\nu_\mathrm{i} + \phi_\mathrm{i})], \quad (5)$$

where ν_i, A_i and ϕ_i are the i=1-29 frequencies, amplitudes and phases reported in Table 3. The amplitudes of the pulsations listed in the top of the table are comparable –or even larger– to the expected eclipse depth. In consequence, instead of considering them purely as noise (Zhang et al. 2018) we carried out a thorough analysis of their impact over the planetary signature. As a counterpart, several pulsations reported in this work have amplitudes smaller than 100 ppm, lying at the limit or even below TESS photometric noise. In consequence, these pulsations might be statistically irrelevant when including them as part of our model budget, which was analyzed, too.

Using Period04, we computed pulsation-free residuals (PFRs) taking into account sub-groups of pulsations, namely the full set, and those with the 25, 20, 15, 10, 9, 8, 7, 6, 5, 4, 3, 2 and 1 highest amplitudes. The difference in step serves as a way to carry out a more detailed investigation of the impact of the pulsations with the highest amplitudes. In this fashion, the last residual data set is computed removing from TESS primary

transit free light curve *only* the frequency with the highest amplitude, and the first one removing all the pulsations. We ended up with 14 PFRs, each one of them with a different "pulsation noise" level. At this point, it is worth to mention that the pulsations of δ Scuti stars are far from being perfect sine functions. Period04 has been developed for years by experts in the field, and is in consequence one of the best tools we have to extract accurate pulsations from photometric time series. As a direct consequence of this, performing time-expensive MCMC fits between photometry and pulsation models to derive the frequencies, amplitudes and phases did not improve the residual noise of the PFRs given by Period04. In consequence, from now on we will work with the PFRs given by Period04 directly.

To test if the chosen number of pulsations has an impact in the determination of the physical properties of WASP-33b, for each one of the 14 PFRs we repeated the same process. Here, we carried out an MCMC fit between the PFRs and the models specified in the previous section. In each case we computed the best-fit parameters and their uncertainties, along with the standard deviation of the residuals (PFRs minus best-fit SEM(t) + PPV(t) model) and the Bayesian Information Criterion, BIC = χ^2 + k ln(N). For the BIC, χ^2 is computed in the usual way, between the PFRs and the best-fit model. N corresponds to the total length of the photometry, and k is the number of fitting parameters. For k we considered the usual four parameters (sf, c_0, c_1 and c_2), plus 3×PN, being PN the number of pulsations considered in each sub-group of PFRs. The factor 3 accounts for each frequency, amplitude and phase.

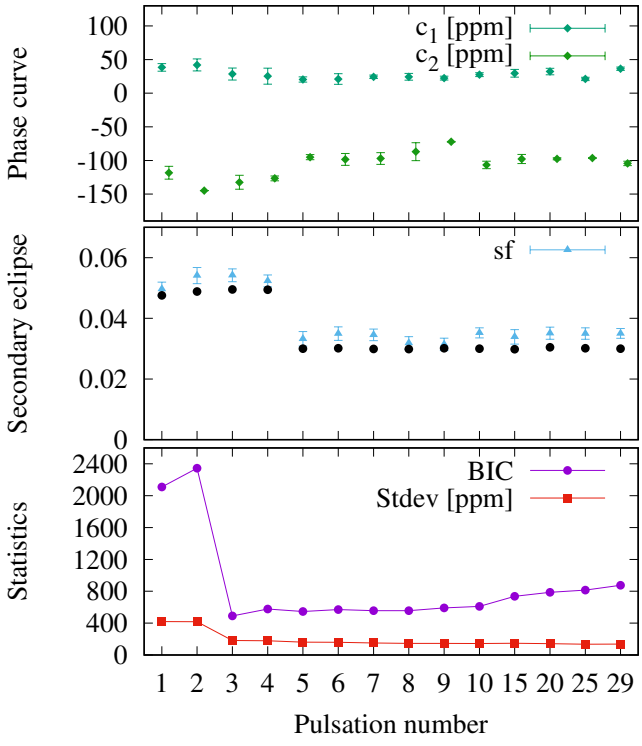

Fig. 6: Evolution of relevant parameters as a function of the number of pulsations considered to remove from the data. From top to bottom: the phase curve coefficients, c_1 and c_2, in green points; the scaling factor in blue triangles; and two statistics, namely the BIC in red circles and the standard deviation of the residual light curves in black squares.

Figure 6 shows the evolution of the BIC, the standard deviation of the residuals, and some of the fitted parameters, specifically sf, c_1 and c_2. These are given as a function of the number of pulsations taken into consideration in the pulsation model. The figure reveals two important aspects. First, a pulsation model that includes the frequencies with the three highest amplitudes favors the minimization of the BIC. However, there is a change of almost 50% in the scaling factor, sf, when the first five frequencies are included. To investigate if this large difference is caused by an inadequate consideration of the pulsations of the host star we proceed as follows. We created 14 light curves using as time stamps those of TESS data, and as model, (SEM(t) + PPV(t))×PM(t). As frequencies, amplitudes and phases we used the ones shown in Table 3, considering them in the same way as the PFRs were produced. As scaling factor, sf, we considered an arbitrary value of 0.03. For c_1 and c_2, 50 and -120 ppm, respectively. Once the synthetic light curves were generated, we fitted them back with the phase curve and secondary eclipse models. The black circles shown on the central panel of Figure 6 reveal the retrieved scaling factors for each one of the synthetic light curves. Not surprisingly, the recovered sf's follow the exact same behaviour as the ones that were obtained from TESS photometry. In consequence, the observed "jump" is consequent to an insufficient treatment of the pulsations of the host star. From PN = 5 and onward, the derived sf is consistent within errors. Among all these, PN = 5 corresponds to the smallest BIC value. In addition to this, the difference between the two smallest BIC values overexceeds the required ΔBIC <-6 (Kass & Raftery 1995), which is a strong evidence in favor of the pulsation model formed solely by the first five pulsations. The remaining pulsations have a negligible impact in the planetary features and are, in consequence, ignored further.

4.2. WASP-33b: primary results

The best-fit secondary eclipse-phase curve model can be seen in Figure 9. The corresponding best-fit values for the derived parameters, along with their uncertainties computed in the usual way from their posterior distributions, are listed in Table 4. Posterior probability distributions for the four parameters can be seen in Figure 7.

The amplitude of the phase curve, A, was computed as:

$$A(c_1, c_2) = \sqrt{c_1^2 + c_2^2}, \quad (6)$$

and the eclipse depth was computed as:

$$ED(sf, R_P/R_S) = sf \times (R_P/R_S)^2. \quad (7)$$

In both cases, their errors were computed from error propagation among the involved parameters.

Figure 9 shows, from top to bottom, TESS photometry of WASP-33 in red points, phase-folded with the best-fit orbital period. Primary transits are around phases $\phi = 0/1$, while the secondary eclipse lies around $\phi = 0.5$. In black continuous line is the best-fit primary transit model. The second panel shows, in red points, TESS photometry once the primary transits and the pulsation model including F1, F10 and F9 were removed. Overplotted in black points are the same data, but binned to $\Delta\phi = 0.01$ (equivalently, Δt~17 minutes). In the center of the figure a dip can be seen, that was not visible in the sub-figure before. The third panel shows a zoom-in to the previous binned data points, along with the best-fit secondary eclipse plus phase

Table 4: Best-fit values and 1-σ uncertainties for the parameters accompanying the phase curve (c_0, c_1 and c_2) and the scaling factor of the secondary eclipse model, sf. In addition, the amplitude of the phase curve, A, the eclipse depth, ED, and the offset between the region of maximum brightness and the sub-stellar point, $\phi_{\rm off}$.

Parameter (ppm)	Best-fit value (this work)
c_0	33.7 ± 8.1
c_1	23.5 ± 10.6
c_2	-96.7 ± 12.3
sf	0.0344 ± 0.0026
A	100 ± 12
ED	425 ± 32
$\phi_{\rm off}$ (°)	-13.6 ± 6.2

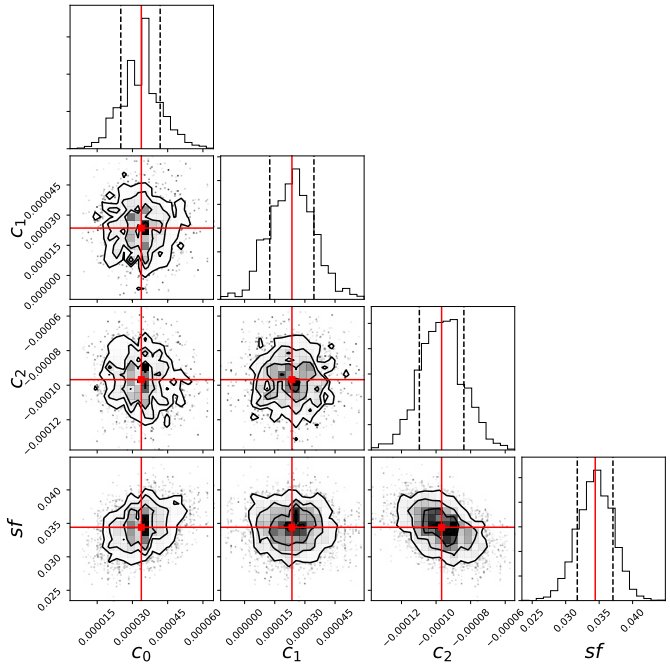

Fig. 7: Posterior distributions for the fitted parameters specified in Table 4.

curve models in black continuous line. The last panel shows the residuals between these two.

4.3. Physical parameters derived from these observations

Following the prescription given by Cowan & Agol (2011), from our derived parameters we computed the bond albedo,

$$A_B = 1 - \frac{5T_n^4 + 3T_d^4}{2T_o^4}, \quad (8)$$

and the heat redistribution efficiency,

$$\epsilon = \frac{8}{5 + 3(T_d/T_n)^4} \quad (9)$$

where T_d and T_n correspond to the temperature of the day-side and the night-side, respectively. Table 5 summarizes them, compared to the ones computed by Zhang et al. (2018).

Table 5: Bond albedo, recirculation efficiency and day and night-side brightness temperatures for WASP-33b within the TESS passband.

Parameter	Value (this work)	Value (Zhang et al. 2018)
A_B	0.239 ± 0.039	$0.25^{+0.09}_{-0.10}$
ϵ	0.191 ± 0.007	$0.22^{+0.05}_{-0.04}$
T_{day} (K)	3184 ± 43	3144 ± 114
T_{night} (K)	1702 ± 22	1757 ± 88

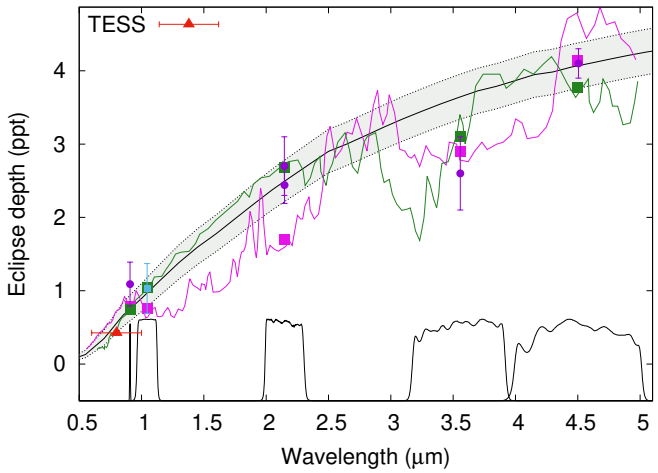

Fig. 8: Eclipse depth, in ppt, as a function of wavelength. The red triangle corresponds to TESS value reported in this work. The gray area shows 1-σ contour of the equilibrium temperature of WASP-33b. Models carbon-rich non-inverted model and solar composition model with an inverted temperature structure are given in green and pink lines, respectively. Models and literature measurements come from Deming et al. (2012) and von Essen et al. (2015).

We obtain uncertainties on all these parameters using the posterior probability distributions for the values c_1, c_2 and sf. In detail, for each one of the 8000 MCMC iterations we compute 8000 bond albedos, recirculation efficiencies, and day and night-side brightness temperatures. In this way, the values reported in Table 5 are obtained from their mean and standard deviation. Our values are fully consistent to the ones reported by Zhang et al. (2018). Figure 8 shows our derived eclipse depth compared to literature measurements. As the figure shows, TESS new addition can not disentangle the presence of temperature inversion in WASP-33b.

5. Conclusion

In this work we present new phase curve and secondary eclipse observations of WASP-33b, obtained analyzing 23 days of TESS photometry. From both the secondary eclipse depth and the amplitude of the phase curve we use a simple model to derive the brightness temperatures, albedo and recirculation efficiency, confirming that WASP-33b behaves as other hot Jupiters, despite being the second hottest planet known so far. Due to the nature of TESS continuous monitoring over WASP-33, we characterize the pulsation spectrum of the host star, finding 29 pulsations with amplitude signal-to-noise ratio higher than 4, instead of the 8 known so far. The newly unveiled low-frequency power spectrum range of the star revealed two pulsations with frequencies

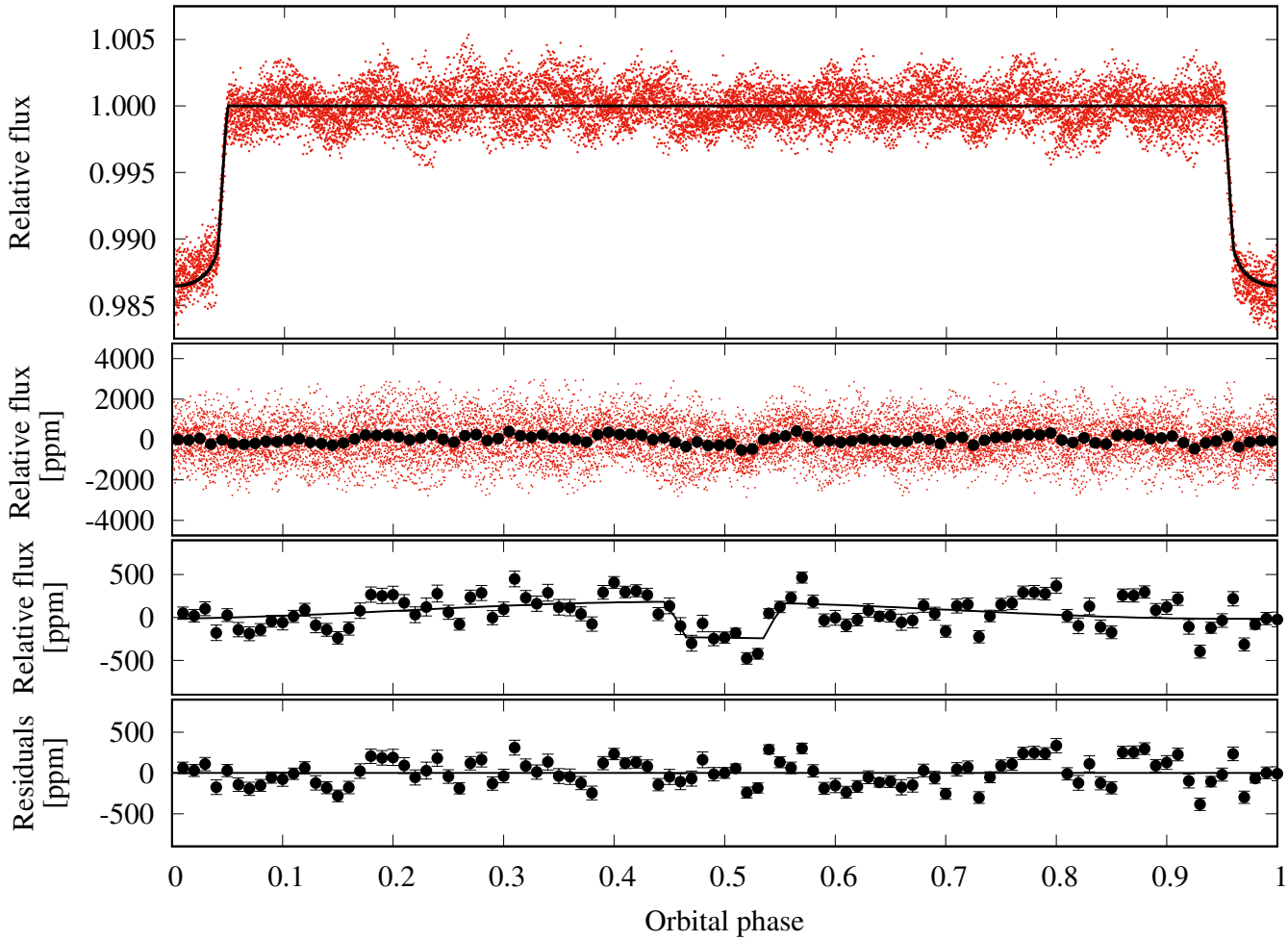

Fig. 9: From top to bottom: phase-folded light curve of WASP-33 in red points showing the primary transit around phases 0,1 and the pulsations of the host star. Black continuous line corresponds to the best-fit primary transit model; Relative flux of WASP-33 in parts per million (ppm) once the pulsations specified in Section 4.1 and the primary transit model were removed. Black circles are the data binned at $\phi = 0.01$; Zoom-in to the black points specified before, in black circles. Overplotted in black continuous line is the best-fit phase curve + secondary eclipse model; Corresponding residuals from the best-fit model.

lower than 3 c/d that are usually observed in γ Doradus stars, making WASP-33 to potentially fall into a γ Doradus/δ Scuti hybrid classification. Paying special attention in the way the pulsations are considered while determining planetary parameters, we find that using solely the minimization of the BIC to quantify the amount of pulsations to be considered in our model does not provide correct planetary parameters. Special care has to be taken into the pulsations with the highest amplitude.

References

Adams, E. R., Dupree, A. K., Kulesa, C., & McCarthy, D. 2013, AJ, 146, 9
Aerts, C., Christensen-Dalsgaard, J., & Kurtz, D. W. 2010, Asteroseismology
Angelov, T. 1996, Bulletin Astronomique de Belgrade, 154, 13
Balona, L. A. & Dziembowski, W. A. 2011, MNRAS, 417, 591
Bouma, L. G., Winn, J. N., Baxter, C., et al. 2019, AJ, 157, 217
Bourrier, V., Kitzmann, D., Kuntzer, T., et al. 2019, arXiv e-prints, arXiv:1909.03010
Breger, M., Handler, G., Garrido, R., et al. 1999, A&A, 349, 225
Breger, M., Handler, G., Nather, R. E., et al. 1995, A&A, 297, 473
Breger, M., Handler, G., Serkowitsch, E., et al. 1996, A&A, 309, 197
Breger, M. & Montgomery, M. 2000, Delta Scuti and Related Stars, Vol. 210
Breger, M., Stich, J., Garrido, R., et al. 1993, A&A, 271, 482
Claret, A. & Bloemen, S. 2011, A&A, 529, A75
Collier Cameron, A., Guenther, E., Smalley, B., et al. 2010, MNRAS, 407, 507
Cowan, N. B. & Agol, E. 2008, ApJ, 678, L129
Cowan, N. B. & Agol, E. 2011, ApJ, 729, 54
Daylan, T., Günther, M. N., Mikal-Evans, T., et al. 2019, arXiv e-prints, arXiv:1909.03000
de Mooij, E. J. W., Brogi, M., de Kok, R. J., et al. 2013, A&A, 550, A54
Deming, D., Fraine, J. D., Sada, P. V., et al. 2012, ApJ, 754, 106
Dragomir, D., Teske, J., Günther, M. N., et al. 2019, ApJ, 875, L7
Gaia Collaboration, Brown, A. G. A., Vallenari, A., et al. 2018, A&A, 616, A1
Grigahcène, A., Antoci, V., Balona, L., et al. 2010, ApJ, 713, L192
Günther, M. N., Pozuelos, F. J., Dittmann, J. A., et al. 2019, Nature Astronomy, 3, 1099
Göttingen, G.-A.-U. 2018, Göttingen Spectral Library by PHOENIX
Hambleton, K. M., Kurtz, D. W., Prša, A., et al. 2013, MNRAS, 434, 925
Haynes, K., Mandell, A. M., Madhusudhan, N., Deming, D., & Knutson, H. 2015, ArXiv e-prints
Herrero, E., Morales, J. C., Ribas, I., & Naves, R. 2011, A&A, 526, L10
Jenkins, J. M. 2017, Kepler Data Processing Handbook: KSCI-19081-002, Tech. rep.
Jenkins, J. M., Twicken, J. D., McCauliff, S., et al. 2016, Society of Photo-Optical Instrumentation Engineers (SPIE) Conference Series, Vol. 9913, The TESS science processing operations center, 99133E
Jones, E., Oliphant, T., Peterson, P., et al. 2001, SciPy: Open source scientific tools for Python, http://www.scipy.org
Kass, R. E. & Raftery, A. E. 1995, Journal of the American Statistical Association, 90, 773
Kostov, V. B., Schlieder, J. E., Barclay, T., et al. 2019, AJ, 158, 32
Lenz, P. & Breger, M. 2005, Communications in Asteroseismology, 146, 53
Mandel, K. & Agol, E. 2002, ApJ, 580, L171

Moya, A., Bouy, H., Marchis, F., Vicente, B., & Barrado, D. 2011, A&A, 535, A110
Mugrauer, M. 2019, MNRAS, 490, 5088
Ngo, H., Knutson, H. A., Hinkley, S., et al. 2016, ApJ, 827, 8
Patil, A., Huard, D., & Fonnesbeck, C. J. 2010, Journal of Statistical Software, 35, 1
Ricker, G. R., Winn, J. N., Vanderspek, R., et al. 2015, Journal of Astronomical Telescopes, Instruments, and Systems, 1, 014003
Rodriguez, J. E., Quinn, S. N., Huang, C. X., et al. 2019, AJ, 157, 191
Shporer, A., Wong, I., Huang, C. X., et al. 2019, AJ, 157, 178
Smith, A. M. S., Anderson, D. R., Skillen, I., Collier Cameron, A., & Smalley, B. 2011, MNRAS, 416, 2096
Uytterhoeven, K., Moya, A., Grigahcène, A., et al. 2011, A&A, 534, A125
Vanderburg, A., Huang, C. X., Rodriguez, J. E., et al. 2019, ApJ, 881, L19
von Essen, C., Cellone, S., Mallonn, M., et al. 2017, A&A, 603, A20
von Essen, C., Czesla, S., Wolter, U., et al. 2014, A&A, 561, A48
von Essen, C., Mallonn, M., Albrecht, S., et al. 2015, A&A, 584, A75
von Essen, C., Stefansson, G., Mallonn, M., et al. 2019, A&A, 628, A115
Wöllert, M. & Brandner, W. 2015, A&A, 579, A129
Wong, I., Benneke, B., Shporer, A., et al. 2019a, arXiv e-prints, arXiv:1912.06773
Wong, I., Shporer, A., Morris, B. M., et al. 2019b, arXiv e-prints, arXiv:1910.01607
Zhang, M., Knutson, H. A., Kataria, T., et al. 2018, AJ, 155, 83

Appendix A: Primary transits photometry of WASP-33b

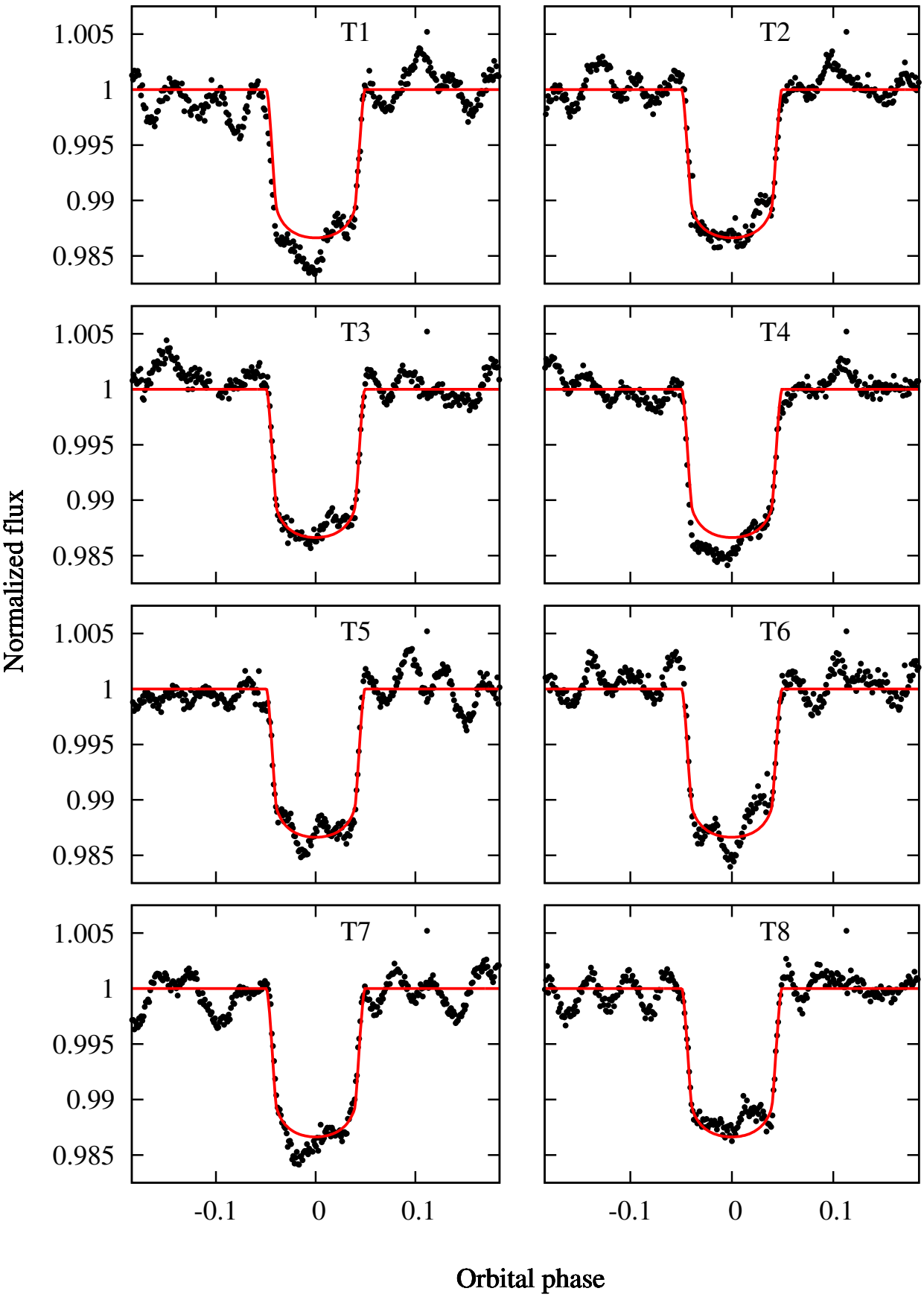

Fig. A.1: Normalized flux as a function of orbital phase for the primary transits of WASP-33b observed by TESS. From top to bottom and left to right time evolves. TESS observations are in black points, and the best-fit model in red continuous line. Individual error bars are not plotted to better visualize the effect of the pulsations over the photometry.

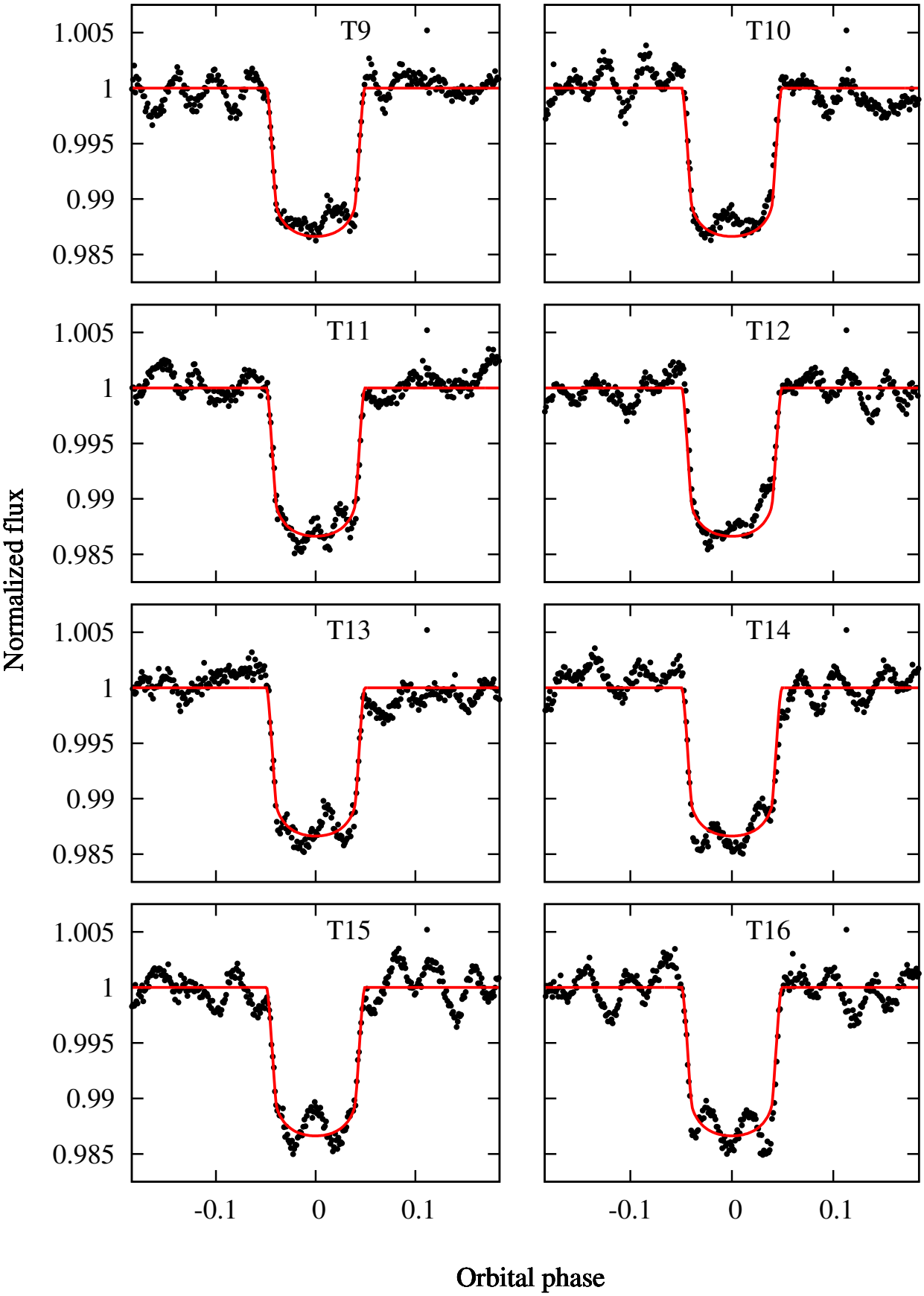

Fig. A.2: Same as Fig. A.1, but for the remaining 8 primary transits.